공학석사학위논문

Numerical Investigation on Three-dimensional Effects of Over-expanded Rocket Nozzle

과팽창 로켓 노즐 유동의 3 차원 효과에 대한 수치해석 연구

2017 년 2 월

서울대학교 대학원

기계항공공학부

문 시 윤

Abstract

Numerical Investigation on Three-dimensional Effects of Over-expanded Rocket Nozzle

Siyoon Moon
Mechanical and Aerospace Engineering
The Graduate School
Seoul National University

In the early stage of liquid rocket engine startup with an over-expanded state, internal flow begins to develop in the form of FSS (Free Shock Separation) which the separated plume stays away from the wall. However, depending on the type of the nozzle shape, a drastic and unpredictable transition occurs to the form of RSS (Restricted Shock Separation) that the separated plume is reattached to the wall surface.

In this research, viscous unsteady two-dimensional axisymmetric and three-dimensional nozzle internal flow analysis using CFD simulations were conducted with a structured-unstructured mixed grid system. Especially, the numerical three-dimensional effects when a transition from FSS to RSS occurs were analyzed changing Nozzle Pressure Ratio (NPR). As a result, it was identified that the transition occurs more slowly in the three-dimensional flow analysis than the axisymmetric two-dimensional case as the NPR increases. And the nozzle wall surface temperature asymmetry phenomenon was identified, and the cause for

it was analyzed. Also, the magnitude of the side load and the moment acting on the neck of the nozzle generated by the asymmetric pressure distribution on a nozzle wall was measured.

Keywords: Computational Fluid Dynamics (CFD), Rocket Nozzle, Overexpansion Flow, Free Shock Separation (FSS), Restricted Shock Separation (RSS), 3-D Effects, Side-Load

Student Number: 2015 - 20768

Table of Contents

List of Figures

List of Tables

Chapter 1

Introduction

1.1 Liquid Rocket Engine Nozzle Side-load

Liquid rocket engine nozzles are designed for high altitude operation. Therefore, under a sea level condition, an overexpansion occurs during the start-up or shut-down processes. However, in ground tests and rocket launching processes that are carried out under such over-expanded flow conditions, rocket launch or test failure cases were reported [1,2].

As a result of grasping the cause, it was verified that the nozzle wall surface side-load occurs in the shape of specific types of nozzles (TOC, TOP types) and it leads to breakage of nozzle structures. It was also found that the side load may apply a moment to the neck of a nozzle and gives a considerable damage to the neck. Since then the problem of side loading of the rocket engine nozzle has become an important design consideration factor.

1.2 Side-load Occurrence Mechanism

The flow separation in the expansion flow inside the liquid rocket engine nozzle can be divided into two patterns. One is Free Shock Separation (FSS)

generated at low pressure ratio and the other is Restricted Shock Separation (RSS) appears as the chamber pressure ratio increases [3]. FSS and RSS have different characteristics. In particular, wall pressure distribution on the downstream of flow separation is formed greatly different.

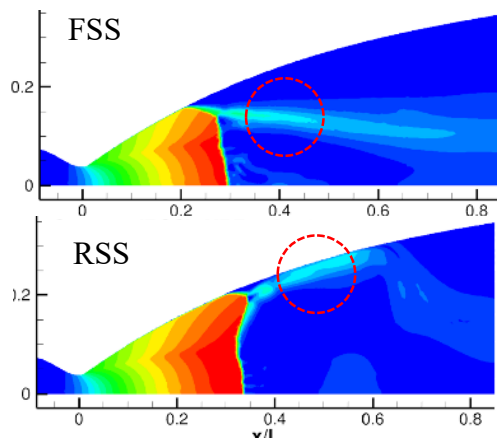

Figure 1.1: FSS (top) and RSS (bottom) Mach contour

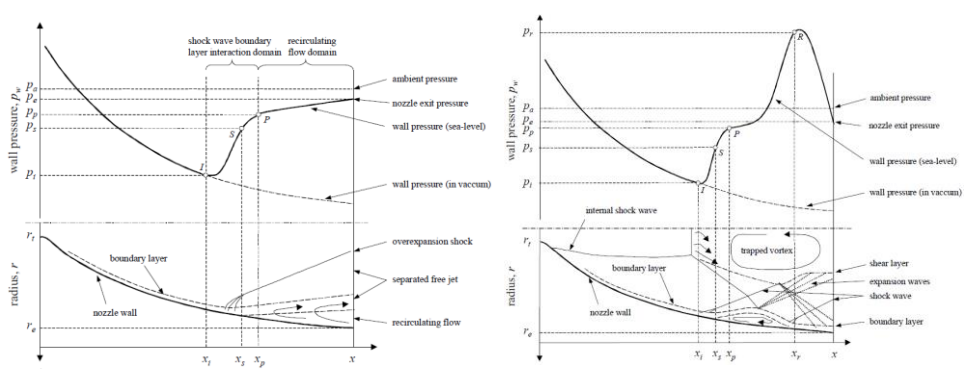

Figure 1.2: Schematics of FSS (left) and RSS (right) features with wall pressure profiles each (up), Ostlund (2002)

1.2.1 Free Shock Separation (FSS)

FSS is a flow separation pattern occurring in all nozzle types. The flow downstream of the separation remains separated from the wall and continues as a free jet. Therefore, the wall pressure behind flow separation shows the similar value as the external atmospheric pressure.

1.2.2 Restricted Shock Separation (RSS)

As the pressure in the chamber increases and flow develops, the radial direction momentum towards the wall is generated by conditions such as internal shock waves and nozzle shape. And the separated flow re-attaches again to the nozzle wall, thus forming a closed separation bubble. This separation pattern is called Restricted Shock Separation (RSS). In this flow, the wall surface pressure after flow separation is seen to oscillate due to such complicated flow phenomenon, and it may form a local peak because of the shock-boundary layer interaction phenomenon at the wall. RSS occurs only in some specific nozzle types (TOP, TOC), depending on the curvature and shape of the neck of the nozzle.

Figure 1.1 shows the flow examples of FSS and RSS each, and the schematics of each separation patterns and the wall pressure distribution are shown in Fig. 1.2 [4].

1.2.3 Asymmetrical flow at the moment of separation pattern transition

As the pressure increases, the flow separation pattern inside the nozzle

changes in the order FSS - RSS - FSS. However, the transition between FSS and RSS occurring in a short time shows an instantaneously asymmetric flow distribution, which induces asymmetric wall pressure distribution. Such an imbalance in the pressure distribution of the wall surface causes the side load on the nozzle wall as a result.

1.3 Objectives of Thesis

So far, many research such as sea-level side loads in high-area-ratio engines, Nave and Coffey [3], separation pattern in the plume of rocket nozzles, Hagemann [5], and Fluid-Structure Interaction (FSI) analysis of full 3-D nozzle flow, Wang [6], were conducted mainly by NASA Marshall Space Flight Center and DLR in relation to liquid rocket engine nozzle over-expanded flow. Like this, there are instances in which axisymmetric two-dimensional flow analysis was intensively interpreted or three-dimensional analysis results are analyzed. However, there has been no research that concentratedly analyzed three-dimensional effects by simultaneously analyzing axisymmetric two-dimensional and three-dimensional cases in the same shape.

Therefore, in this research, the three-dimensional effects of supersonic nozzle internal flow were investigated using Computational Fluid Dynamics (CFD) with the unsteady RANS analysis of 2-D axisymmetric and full 3-D nozzle flow using a structured-unstructured mixed grid system. Specifically, the flow pattern variation while increasing the Nozzle Pressure Ratio (NPR), and some

three-dimensional effects were studied including the transition tendency change of the two and three-dimensional flow separation.

Chapter 2

Numerical Method

2.1 Governing Equation

The governing equations are the three-dimensional compressible Navier-Stokes equation, which can be written in a conservative form as follows:

$$\frac{\partial \rho}{\partial t} + \frac{\partial}{\partial x_j}\left(\rho u_j\right) = 0 \tag{2.1}$$

$$\frac{\partial}{\partial t}\left(\rho u_i\right) + \frac{\partial}{\partial x_j}\left(\rho u_j u_i\right) = -\frac{\partial p}{\partial x_i} + \frac{\partial \hat{\tau}_{ij}}{\partial x_j} \tag{2.2}$$

$$\frac{\partial \rho e_t}{\partial t} + \frac{\partial}{\partial x_j}\left(\rho u_i e_t\right) = -\frac{\partial p u_j}{\partial x_i} + \frac{\partial}{\partial x_j}\left[u_i \hat{\tau}_{ij} - q_j\right] \tag{2.3}$$

where e_t represents the total energy, and $\hat{\tau}_{ij}$ are composed of molecular and Reynolds stresses.

$$\hat{\tau}_{ij} = 2\mu\left(S_{ij} - \frac{1}{3}S_{kk}\delta_{ij}\right) + \tau_{ij} \tag{2.4}$$

$$\tau_{ij} = 2\mu_t\left(S_{ij} - \frac{1}{3}S_{kk}\delta_{ij}\right) - \frac{2}{3}\rho k\delta_{ij} \tag{2.5}$$

$$S_{ij} = \frac{1}{2}\left(\frac{\partial u_i}{\partial x_j} + \frac{\partial u_j}{\partial x_i} \right) \tag{2.6}$$

where $\hat{\tau}_{ij}$ is the summation of laminar and turbulent stresses, and τ_{ij} is the turbulent stress term. The velocity strain rate tensor is represented by S_{ij}, and k is the turbulent kinetic energy. The quantity μ is the molecular viscosity determined by the Sutherland law, and μ_t is the turbulent eddy viscosity. Note that the Boussinesq approximation is assumed to introduce Eq. 2.5. The total heat flux rate q_j is defined as

$$q_j = -\left(\frac{\gamma}{\gamma - 1} \right)\left(\frac{\mu}{\mathrm{Pr}} + \frac{\mu_t}{\mathrm{Pr}_t} \right)\frac{\partial T}{\partial x_j} \tag{2.7}$$

where γ is the ratio of specific heats, and the variables Pr and Pr_t are the laminar and turbulent Prandtl number, respectively.

The perfect gas equation of state is introduced to the pressure as follows:

$$p = \rho(\gamma - 1)\left(e - \frac{1}{2} u_i u_i \right) \tag{2.8}$$

The three-dimensional compressible Navier-Stokes equations are implemented on the flow solver and it can be expressed in an integral form as seen

in the following equation:

$$\frac{\partial}{\partial t}\int_{\Omega}\vec{Q}\,d\Omega+\oint_{\partial\Omega}(\vec{F}_c-\vec{F}_v)\,dA=\int_{\Omega}\vec{S}\,d\Omega \tag{2.9}$$

The $\vec{Q}$ vector represents the conservative variables. The $\vec{F}_c$ and $\vec{F}_v$ represent the convective and viscous flux respectively. The $\vec{S}$ indicates the source term.

$$Q=\left[\rho,\ \rho u,\ \rho v,\ \rho w,\ \rho e_t\right]^T \tag{2.10}$$

$$\overrightarrow{F_c}=\left[\rho V,\ \rho uV+n_x p,\ \rho vV+n_y p,\ \rho wV+n_z p,\ \rho HV\right]^T \tag{2.11}$$

$$\overrightarrow{F_v}=\begin{bmatrix}0\\ n_x\tau_{xx}+n_y\tau_{yx}+n_z\tau_{zx}\\ n_x\tau_{xy}+n_y\tau_{yy}+n_z\tau_{zy}\\ n_x\tau_{xz}+n_y\tau_{yz}+n_z\tau_{zz}\\ n_x\theta_x+n_y\theta_y+n_z\theta_z\end{bmatrix} \tag{2.12}$$

where,

$$\theta_x=u\tau_{xx}+v\tau_{xy}+w\tau_{xz}-q_x$$

$$\theta_y=u\tau_{yx}+v\tau_{yy}+w\tau_{yz}-q_y$$

$$\theta_z=u\tau_{zx}+v\tau_{zy}+w\tau_{zz}-q_z$$

and V indicate contravariant velocity vector as

$$V\equiv\vec{v}\cdot\vec{n}=n_x u+n_y v+n_z w$$

2.2 Turbulence Modeling

For an adequate description of turbulent flow field within the framework of a Reynolds Averaged Navier-Stokes (RANS) formulation, Menter's $k-\omega$ Shear Stress Transport (SST) model is employed. This turbulence model is composed of two transport equations of the turbulent kinetic energy and the dissipate rate.

2.2.1 The Menter's k-ω SST Two-Equation Model

The $k-\omega$ model performs well and is superior to the $k-\varepsilon$ model within the laminar sub-layer. However, the $k-\omega$ model has been shown to be influenced strongly by the specification of the free-stream value of ω outside the boundary layer. There, the $k-\omega$ model does not appear to be an ideal model for applications in the wake region of the boundary layer. On the other hand, the $k-\varepsilon$ model behaves superior to that of the $k-\omega$ model in the outer portion and wake regions of the boundary layer, but inferior in the inner region of the boundary layer. To include the best features of each model, Menter has combined different elements of the $k-\varepsilon$ and $k-\omega$ models to form a new two-equation model. This model incorporates the $k-\omega$ model for the inner region of the boundary layer, and it switches to the $k-\varepsilon$ model for the outer and wake region of the boundary layer [7].

The original $k-\omega$ model is multiplied by a function F_1 and the

transformed $k-\varepsilon$ model by a function $(1-F_1)$. The blending function F_1 is set to be one in the near wall region and zero far away from the wall surface. Both the models are combined as:

$$\frac{\partial \rho k}{\partial t}+\frac{\partial}{\partial x_j}\left(\rho u_j k\right)=P-\beta^* \rho \omega k+\frac{\partial}{\partial x_j}\left[\left(\mu+\sigma_k \mu_t\right)\frac{\partial k}{\partial x_j}\right] \tag{2.13}$$

$$\begin{aligned}\frac{\partial \rho \omega}{\partial t}+\frac{\partial}{\partial x_j}\left(\rho u_j \omega\right)=\rho\frac{\gamma}{\mu_t}P-\beta\rho\omega^2+\frac{\partial}{\partial x_j}\left[\left(\mu+\sigma_\omega \mu_t\right)\frac{\partial \omega}{\partial x_j}\right] \\ +2(1-F_1)\frac{\rho\sigma_{\omega 2}}{\omega}\frac{\partial k\partial\omega}{\partial x_j \partial x_j}\end{aligned} \tag{2.14}$$

The constants appearing in Eq. 2.13-14 are evaluated in the following relation by using the blending function.

$$\Phi=F_1\Phi_1+\left(1-F_1\right)\Phi_2 \tag{2.15}$$

where Φ_1 represents the constants associated with the $k-\omega$ model, and Φ_2 represents the constants associated with the $k-\varepsilon$ model and the constants for Φ are specified as follows:

$$\begin{gathered}\gamma_1=\beta_1/\beta^*-\sigma_{\omega 1}\kappa^2/\sqrt{\beta^*},\ \ \gamma_2=\beta_2/\beta^*-\sigma_{\omega 2}\kappa^2/\sqrt{\beta^*} \\ \sigma_{k1}=0.85,\ \ \sigma_{k2}=1.0,\ \ \sigma_{\omega 1}=0.5,\ \ \sigma_{\omega 2}=0.856 \\ \beta^*=0.09,\ \ \beta_1=0.075,\ \ \beta_2=0.0828,\ \ \kappa=0.41\end{gathered} \tag{2.16}$$

In addition, F_1 is a switching function from the $k-\omega$ model to the $k-\varepsilon$ model based on the distance from the nearest solid surface and defined as follows:

$$F_1 = \tanh\left\{\left(\min\left[\max\left[\frac{\sqrt{k}}{\beta^* \omega y}, \frac{500v}{\omega y^2}\right], \frac{4\rho\sigma_{w2}k}{CD_{k\omega}y^2}\right]\right)^4\right\} \tag{2.17}$$

where y is the distance to the nearest surface and $CD_{k\omega}$ is the positive portion of the cross-diffusion term

$$CD_{k\omega} = \max\left[2\rho\sigma_{\omega 2}\frac{1}{\omega}\frac{\partial k}{\partial x_j}\frac{\partial \omega}{\partial x_j}, 10^{-20}\right] \tag{2.18}$$

The eddy viscosity is defined to limit the turbulent shear stress as

$$\mu_t = \frac{\rho k/\omega}{\max\left[1, \Omega F_2 / a_1 \omega\right]}, \quad a_1 = 0.31 \tag{2.19}$$

where Ω is the absolute value of the vorticity and F_2 is included to prevent singular behavior in the free-stream where Ω goes to zero and given by

$$F_2 = \tanh\left\{\left(\max\left[2\frac{\sqrt{k}}{\beta^* \omega y}, \frac{500\mu}{\rho\omega y^2}\right]\right)^2\right\} \tag{2.20}$$

Note that it is recommended to employ the production limiter, which replaces the term of P in the k-equation by

$$P = \tau_{ij}\frac{\partial u_i}{\partial x_j} = \min\left(P, 20\beta^* \omega k\right) \tag{2.21}$$

The boundary conditions and free-stream values are given as follows:

$$\begin{aligned} &\frac{U_\infty^2}{10^5\,\mathrm{Re}_L} < k_{far-field} < \frac{U_\infty^2}{10\,\mathrm{Re}_L} \\ &\frac{U_\infty}{L_{far-field}} < \omega_{far-field} < \frac{10U_\infty}{L_{far-field}} \\ &k_{wall} = 0, \quad \omega_{wall} = \frac{60\nu}{\beta_1\left(\Delta d\right)^2} \end{aligned} \tag{2.22}$$

The $L_{far-field}$ is the approximate length of the computational far-field domain from the wall, and a free-stream turbulent viscosity μ_t has a value between 10^{-5} and 10^{-2} times the free-stream laminar viscosity. The Δd is the distance of the first point away from the wall.

2.3 Spatial Discretization Method

The governing equations can be decomposed to the inviscid flux term and the viscous flux term. The inviscid flux terms are discretized with a finite volume method based on the cell-centered approach.

And because they are in central-differenced forms and are non-dissipative by themselves, the inviscid fluxes should be modified to the cell surface fluxes by explicitly adding the numerical dissipation term. In this study, the flux scheme of RoeM [8] is used for the spatial discretization.

2.3.1 RoeM Scheme

Widely used in the field of compressive fluid analysis Roe's FDS does not have the sole solution at expansion wave analysis and has a problem of selecting a solution with negative entropy. In addition, there is a disadvantage that a carbuncle problem, which is a typical numerical instability phenomenon near the shock wave, is displayed. RoeM scheme analyzes Roe scheme in the form of numerical viscosity term of density and pressure and introduces functions f, g based on the Mach number that adjusts its size according to the direction of the shock wave. As a result, RoeM scheme solves numerical instability problem displayed by Roe's FDS. The numerical flux $H_c^{RoeM}(\bar{Q}_L, \bar{Q}_R)$ of the RoeM scheme is summarized as follows:

$$H_c^{RoeM}(\bar{Q}_L,\bar{Q}_R)=\frac{b_1\times F_c(\bar{Q}_L)-b_2\times F_c(\bar{Q}_R)}{b_1-b_2}+\frac{b_1\times b_2}{b_1-b_2}\Delta Q^* - g\frac{b_1\times b_2}{b_1-b_2}\times\frac{1}{1+\left|\hat{M}\right|}B\Delta Q \tag{2.23}$$

where

$$\Delta Q^* = \rho,\rho u,\rho v,\rho w,\rho H\ ^T,$$

$$B\Delta Q=\left(\Delta\rho-f\frac{\Delta p}{\hat{c}^2}\right)\begin{pmatrix}1\\ \hat{u}\\ \hat{v}\\ \hat{w}\\ \hat{H}\end{pmatrix}+\rho\begin{pmatrix}0\\ \Delta u-n_x\Delta V\\ \Delta v-n_y\Delta V\\ \Delta w-n_z\Delta V\\ \Delta H\end{pmatrix},$$

$$b_1=\max(0,\hat{U}+\hat{c},U_R+\hat{c}),\qquad b_2=\min(0,\hat{U}-\hat{c},U_R-\hat{c})$$

b_1 and b_2 are approximations of the wave velocity and were introduced to overcome the entropy problem near the expansion wave. The Mach number-based functions f and g for adjusting the numerical viscosity term are defined as follows:

$$f=\begin{cases}1 & \hat{u}^2+\hat{v}^2+\hat{w}^2=0\\ \left|\hat{M}\right|^h & elsewhere\end{cases},$$
$$h=1-\min_{e_{mn}\in T_L\cup T_R}\left(\frac{p_m}{p_n},\frac{p_n}{p_m}\right), \tag{2.24}$$

$$g=\begin{cases}\left|\hat{M}\right|^{1-\min\left(\frac{p_m}{p_n},\frac{p_n}{p_m}\right)} & \hat{M}\neq 0\\ 1 & \hat{M}=0\end{cases},$$

The term expressed as the above formula ϕ is Roe's average and the definition is as follows:

$$\begin{aligned}\hat{\rho}&=\sqrt{\rho_L\rho_R}\\ \hat{\phi}&=\frac{\phi_L\sqrt{\rho_L}+\phi_R\sqrt{\rho_R}}{\phi_L+\phi_R},\quad \phi=u,v,w,H\end{aligned} \tag{2.25}$$

2.3.2 Higher-Order Spatial Accuracy

In order to obtain higher order spatial accuracy, a Monotone Upstream-centered Schemes for Conservation Laws (MUSCL) [9] is adopted as:

$$\begin{aligned}U_L&=U_i+\frac{1}{4}\left[(1+\hat{\kappa})\Delta_+ +(1-\hat{\kappa})\Delta_-\right]U_i\\ U_R&=U_j-\frac{1}{4}\left[(1+\hat{\kappa})\Delta_- +(1-\hat{\kappa})\Delta_+\right]U_j\end{aligned} \tag{2.26}$$

where,

$$\begin{aligned}\Delta_+U_i&=U_j-U_i & \Delta_-U_i&=U_i-U_{i'}\\ \Delta_+U_j&=U_{j'}-U_j & \Delta_-U_i&=U_j-U_i\end{aligned}$$

and U denotes the primitive variables. With the constant $\kappa=1/3$, the order of

spatial accuracy is one-third, and the second order of accuracy is achieved with κ=-1, 0, 1. Especially at κ=1, it becomes a central, different scheme of the second order. Values of the primitive variables at the cell interface are modified by extrapolation, which causes an oscillation near the physical discontinuities. To suppress this overshoot phenomenon of the solution, several limiters can be applied by multiplying a function ϕ to the each gradient.

2.4 Time Integration Method

In this study, the 3rd order explicit TVD-RK method was used for main unsteady analyses. In some steady problems such as validation cases, the implicit LU - SGS method [10] were used. Specific equations about 3rd order TVD-RK method are as follows:

2.4.1 3rd order TVD Runge-Kutta scheme

$$\begin{aligned}
\bar{Q}_i^{(1)} &= \bar{Q}_i^n - \frac{\Delta t}{|T_i|} R_i(\bar{Q}, t) \\
\bar{Q}_i^{(2)} &= \frac{3}{4}\bar{Q}_i^n + \frac{1}{4}\bar{Q}_i^{(1)} - \frac{1}{4}\frac{\Delta t}{|T_i|} R_i(\bar{Q}, t+\Delta t) \\
\bar{Q}_i^{(3)} &= \frac{1}{3}\bar{Q}_i^n + \frac{2}{3}\bar{Q}_i^{(2)} - \frac{2}{3}\frac{\Delta t}{|T_i|} R_i(\bar{Q}, t+\frac{1}{2}\Delta t)
\end{aligned} \tag{2.27}$$

Chapter 3

Solver Validations

3.1 Mach 5 Shock Wave Boundary Layer Interaction

The flow structure of FSS and RSS patterns generated in the nozzle are closely related to the shock wave - boundary layer interaction phenomenon. Detailed flow feature of RSS, for example, is shown in Fig. 3.1 [5].

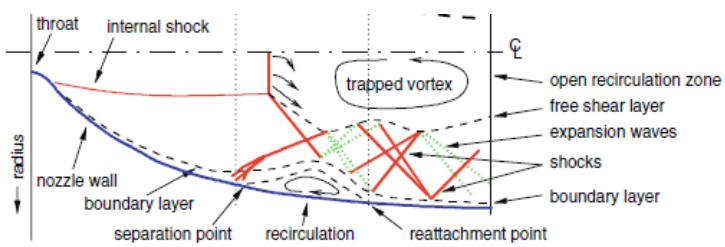

Figure 3.1: Characteristics for Restricted Shock Separation (RSS) pattern

Therefore, a verification of the program was conducted for two-dimensional flow analysis through Mach 5 shock wave boundary layer interaction problem [11] provided by NPARC (National Project for Application-oriented Research in CFD) Archive. The analysis conditions and grid are shown in Table 3.1, 3.2, and Fig. 3.2. The results executed in NASA Wind - US and the Mach contour done in this study were similar as shown in Fig 3.3. Also, the skin friction occurring on the wall around the separation bubble caused by the interaction between the shock

wave and the boundary layer also showed a tendency to agree in Fig. 3.4.

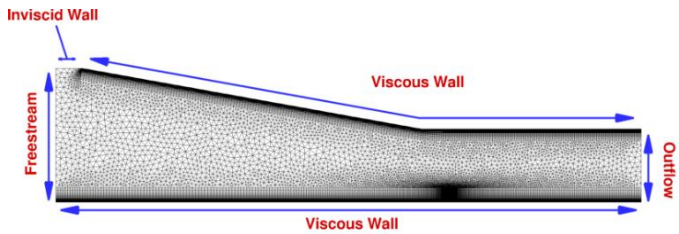

Figure 3.2: Grid and boundary conditions of Mach 5 validation problem

	Total pressure (MPa)	Total temperature (K)	Mach number
Freestream	**2.12**	**410**	**5.0**

Table 3.1: Flow conditions of Mach 5 validation problem

	Current Study	Wind-US
Time integration	Implicit LU-SGS	Implicit UGauss
Spatial discretization	AUSMPW+	HLLE
Limiter	MLP-u2	DQ limiter
Turbulence model	Menter's K - ω SST (2003)	Menter's K - ω SST (2003)

Table 3.2: Algorithm Settings comparison of Mach 5 validation problem

NASA Wind-US	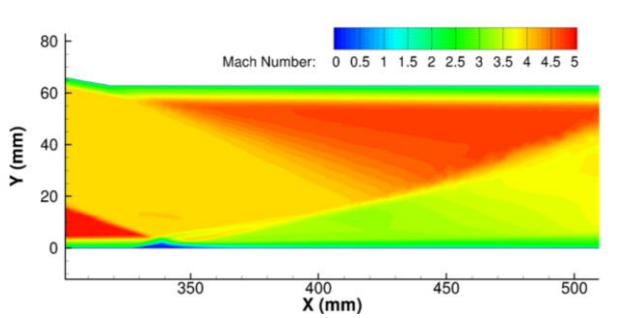
Current Study	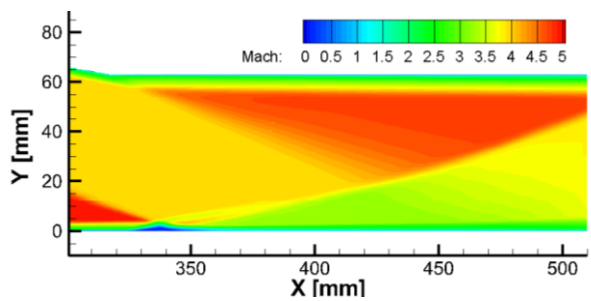

Figure 3.3: Mach contours comparison between provided result (Wind-US) and current study

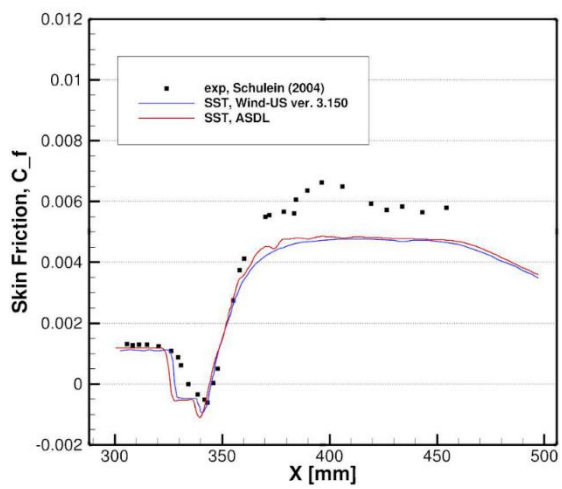

Figure 3.4: Skin friction coefficient comparison between Wind-US and current study

3.2 Seiner Nozzle with Mach 2.0, Heated Jet Flow

The next is the 'Seiner nozzle with Mach 2.0, heated jet flow' problem [12], which is also provided by NPARC Archive. This nozzle problem was chosen as a validation case of the three-dimensional flow analysis program. The flow conditions are as follow Table 3.3, 3.4 and the grid used is shown in Fig. 3.5.

	Total pressure (Pa)	**Total temperature (K)**	**Mach number**
Jet inflow	**793034.98**	**313.14**	**N/A**
Freestream	**101352.93**	**294.44**	**0.01**

Table 3.3: Flow conditions of the Seiner nozzle validation problem

	ASDL	**Wind-US**
Time integration	Implicit LU-SGS	Implicit UGauss
Spatial discretization	AUSMPW+	HLLE
Limiter	MLP-u2	DQ limiter
Turbulence model	Menter's K - ω SST (2003)	Menter's K - ω SST (2003)

Table 3.4: Algorithm Settings comparison of Seiner validation problem

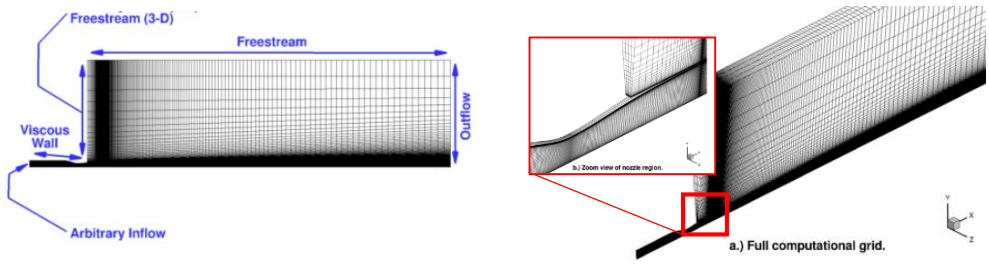

Figure 3.5: Boundary conditions and grid of Seiner nozzle validation problem

The axial velocity component of the cross section and the turbulent kinetic energy contour shows the same trend as Wind-US and current study result in Fig 3.6. Also, the axial velocity component at the nozzle axis position and the graph of the turbulent kinetic energy almost match showing Fig 3.7.

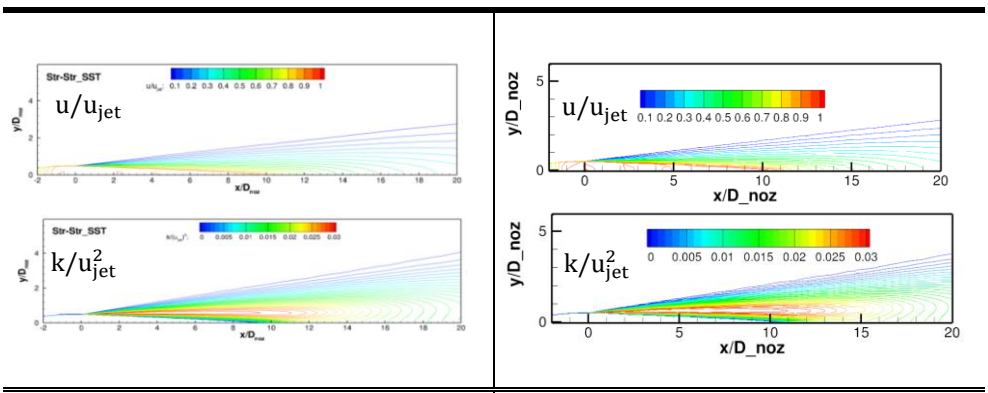

Wind-US	Current study

Figure 3.6: Normalized axial velocity and kinetic energy contour comparison between Wind-US and current study

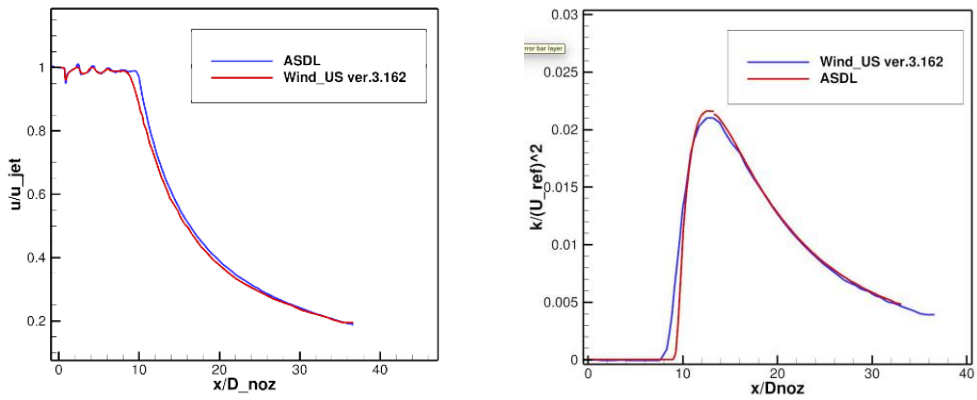

Figure 3.7: Normalized axial velocity (left) and kinetic energy (right) profile comparison between Wind-US and current study

Chapter 4

Preliminary Works Before Analyzing

First, detailed specifications of the rocket engine nozzle are as shown in the following table. And every experimental data in this chapter was conducted by the joint research institute.

Contents	Details	
Specific Feature of the Nozzle	Area ratio	94.5
	Nozzle type	Thrust Optimized Parabolic (TOP)
Material Properties of the Combustion Gas	γ, C_P, μ, k polynomial $f(T)$	
Chamber Inner Condition	$P_{total} = 70\ bar$ $T_{total} = 3642.69K$	
Nozzle External Condition	Ideal gas pressure and temperature at sea level (Same material property as combustion gas)	

* **Experiment was conducted by the joint research institute**

Table 4.1: Liquid rocket engine nozzle specifications

4.1 Combustion Gas Material Property Modeling

To use some coefficients based on temperature, the least-square polynomial

curve fitting was performed using data of points obtained from joint research institute through Chemical Equilibrium with Applications (CEA). The heat capacities, viscosity, and heat conduction coefficients expressed by polynomials of temperature are modeled, and the graph for them are displayed as Fig. 4.1. The specific heat ratio was calculated based on the heat capacity and fixed gas constant R = 360.4 $J/kg \cdot K$

Coefficient	Order
Heat Capacity (C_p)	3rd order
Viscosity (μ)	1st order
Conductivity (k)	1st order

Table 4.2: Orders of least-square curve fitted polynomial equations

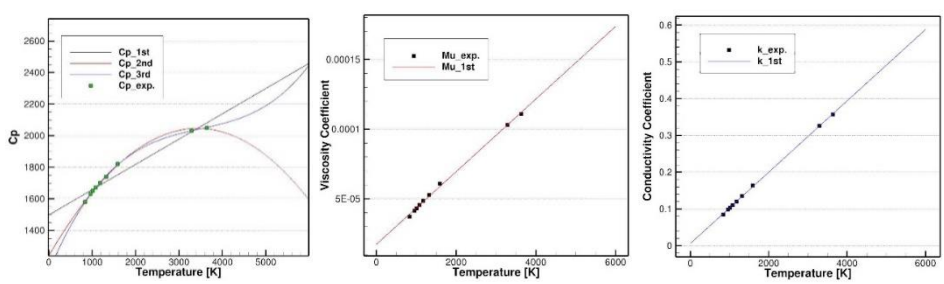

Figure 4.1: Heat capacity, viscosity, and conductivity data curve fit by least square

4.2 Grid Refinement Test for Unsteady Analysis

The point of occurrence of the transition is related to the position of flow separation. Therefore, a grid refinement test was performed depending on how the separation point moves through the unsteady 2-D axisymmetric analysis. The

pressure was increased at a constant rate (70 bar / 0.05 s) and results applying fine, medium and coarse grid were compared. The separation points variation by NPR is shown in Fig. 4.2 for each grid.

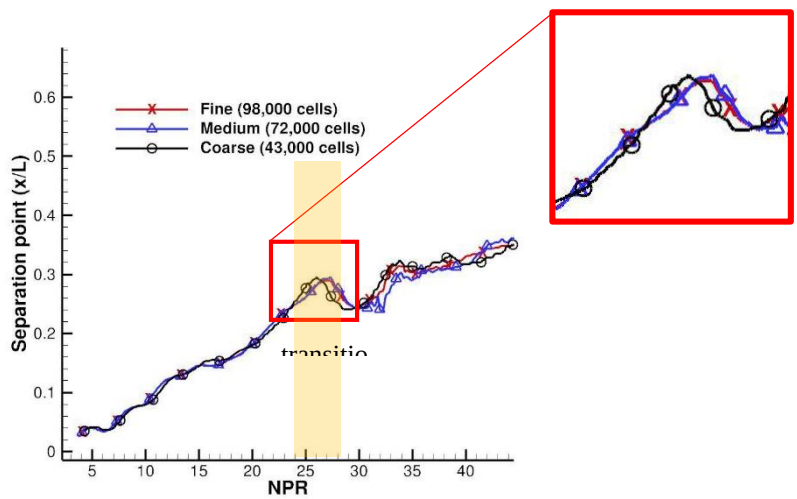

Figure 4.2: Grid refinement test with separations point by NPR

As a result of comparing the separation points of each grid mainly around where the transition occurs, it was found that all results are coincident with the overall trend, but the medium is closer to the fine grid than the course one. Therefore, a medium (≈ 72,000 cells) grid was used for the 2-D axisymmetric analysis.

However, considering a very small time step and the small grid scale in the 3D analysis, the course grid (≈ 43,000 cells) which is the trend coincide with the medium and the fine grid was selected and it rotated 30 times to circumferential direction for efficiency. Therefore, about 1.3 million cells were used for full 3-D

analysis. Used 2-D axisymmetric and 3-D grids are shown in Fig 4.3.

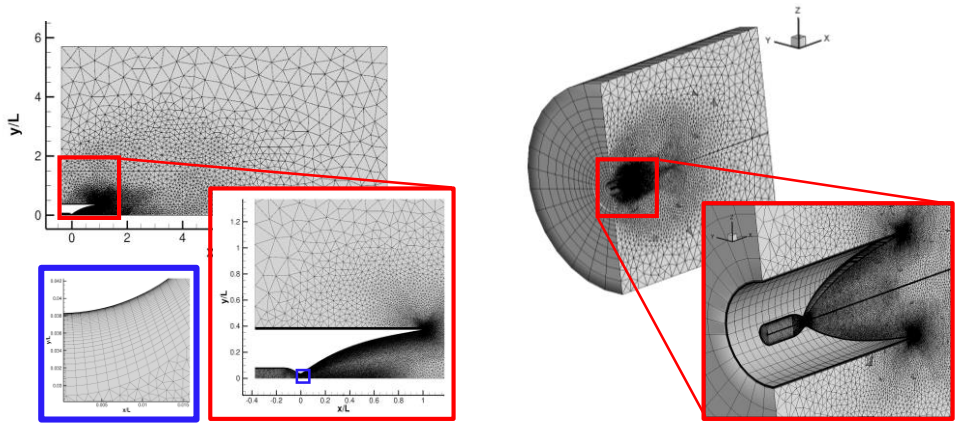

Figure 4.3: 2-D axisymmetric and full 3-D grid used

4.3 Comparison with Experiments

Experimental results with a supersonic diffuser mounted behind the nozzle were compared with the 2-D axisymmetric CFD results performed under the above application conditions. Considering the calculation efficiency and the supersonic flow condition inside the nozzle, computational domain wasn't set behind the nozzle exit and applied supersonic outflow condition at the exit. The wall pressure point data measured on different two lines opposite to each other obtained by the experiment were compared with the wall pressure in the CFD analysis. And as a result, the maximum error was 3.82%, which showed a general tendency to agree well. Figure 4.4 shows the Mach contour and the wall pressure data comparison.

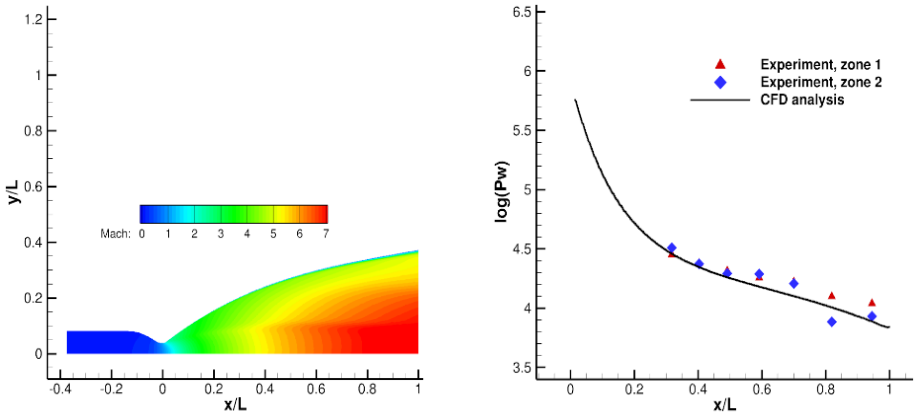

Figure 4.4: Flow Mach contour (left) and the wall pressure comparison with experimental data (right)

4.4 2-D Axisymmetric Steady Analysis

Before the unsteady analysis was taken, to check the NPR range where the transition from FSS to RSS occurs, steady two-dimensional axisymmetric analysis was conducted. After the steady analysis applying the five NPRs of 10, 20, 25, 30, and 40, it was predicted that FSS - RSS transition might occur from about 20 to 25 NPR.

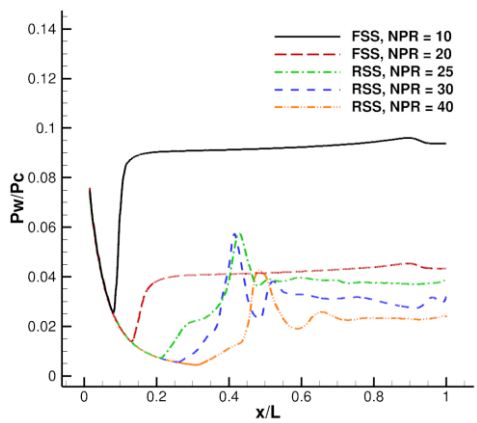

Figure 4.5: Wall pressure profiles of various NPR conditions

4.5 Selection of Pressure-time Slope

In order to observe the transition appearance more accurately, the change rate of pressure over time was applied by transient analysis. However, the slope level similar to the pressure-time increment applied in the experiment is very time-consuming to analyze. Therefore, efficient slope which barely affects the transition process was found as follow.

Figure 4.6 is a graph of pressure-time slope provided in the experiment, and the slope is called T (70bar/0.5s) in this study. And for efficiency, the results obtained by applying 10T (70bar/0.05s) and 20T (70bar/0.025s) were compared with T around the flow separation point. Figure 4.7 shows a brief graph of T, 10T, and 20T.

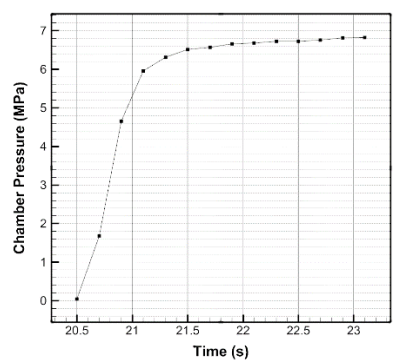

Figure 4.6: Experimental time variation plot for rocket engine nozzle start-up, experiment

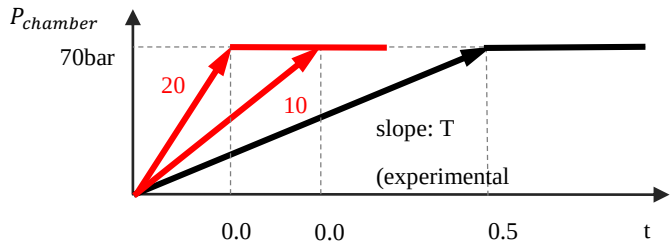

Figure 4.7: Unsteady time variation plot for rocket engine nozzle start-up simulation

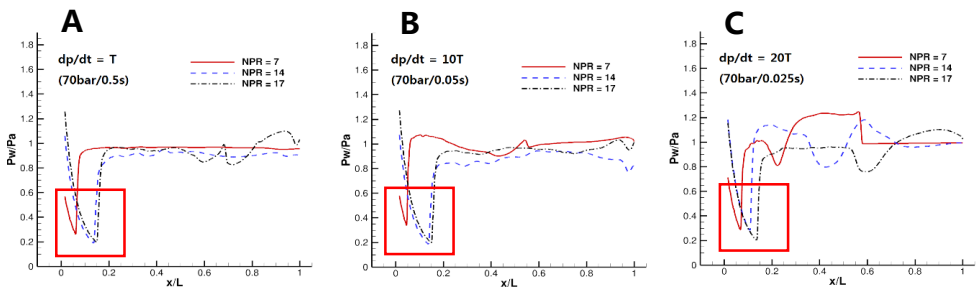

Figure 4.8: Wall pressure profiles for different pressure-time increment (A: T, B: 10T, C: 20T)

In the case of 10T (B) as a result of the comparison, according to the Fig 4.8 and 4.9, the vibration occurring inside the combustion chamber at the beginning of startup damped down before the transition. Also, the flow separation and the shock wave point were almost in agreement with the case of T (A).

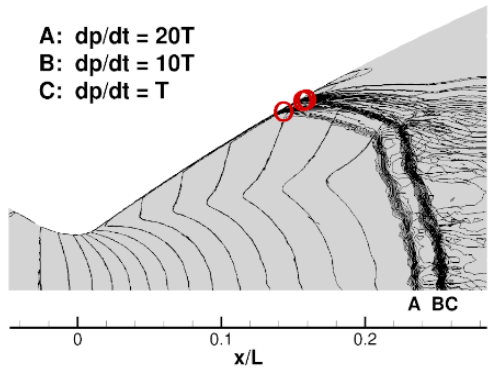

Figure 4.9: Shock and separation positions at NPR = 17

However, in the case of 20T (C), a transition occurred before the vibration of the initial combustion chamber disappears, so it affected and interfered the smooth transition from FSS to RSS. For this reason, the slope case of 10T (B) was chosen.

Chapter 5

Results & Discussion

5.1 Transition NPR range Difference between 2-D & 3-D results

5.1.1 2-D axisymmetric unsteady RANS results

The two-dimensional axisymmetric engine nozzle start-up process was analyzed, and the pressure-time slope was set to 10 T. Figure 5.1 shows the unsteady time variation during the simulation.

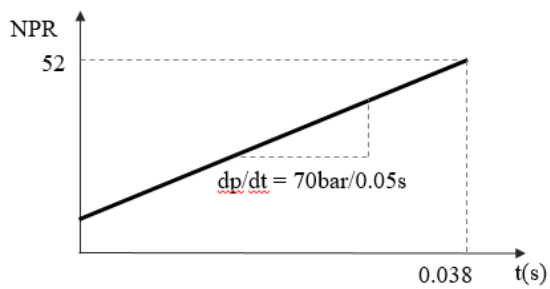

Figure 5.1: Unsteady time variation plot for FSS/RSS transition simulation

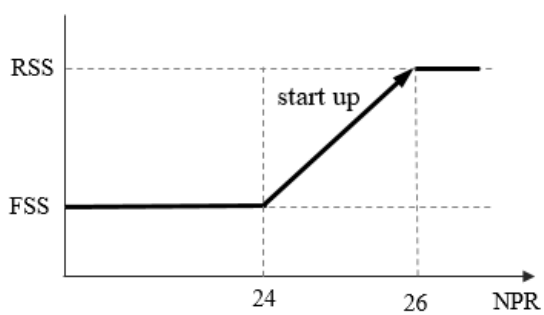

Figure 5.2: Transition occurrence NPR range

NPR was increased to about 52 in 2-D unsteady analysis, taking into consideration that the transition occurs in about 20 to 25 with steady analysis. And it was confirmed that the FSS-RSS transition occurs in the NPR range about 24 to 26. Transition occurrence NPR range is shown in Fig 5.2 and Mach field snapshots with wall pressure distribution profiles during start-up process is shown in Fig. 5.3.

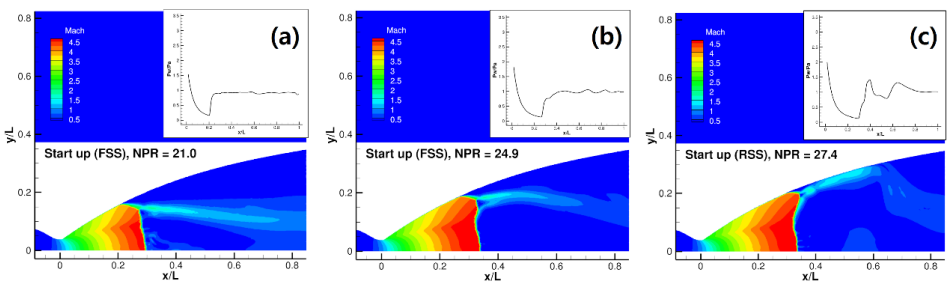

Figure 5.3: Sequence of Mach field snapshots during nozzle start-up (NPR = 21.0 (left), NPR = 24.9 (middle), NPR = 27.4 (right))

5.1.2 3-D unsteady RANS results

Similarly, the startup process was analyzed up to NPR = 35 in 3-D. A transition occurred at about NPR = 28, and pressure asymmetry occurred. It is noteworthy that the transition NPR does not match with the axisymmetric two-dimensional case.

NPR	Mach contour	Wall pressure profiles
25	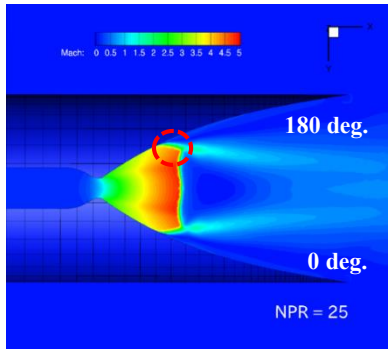	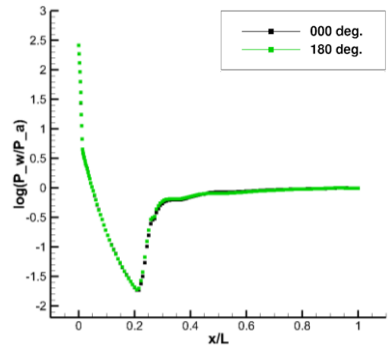
28	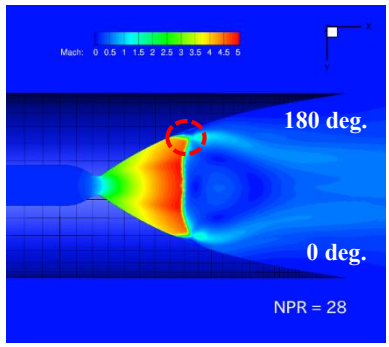	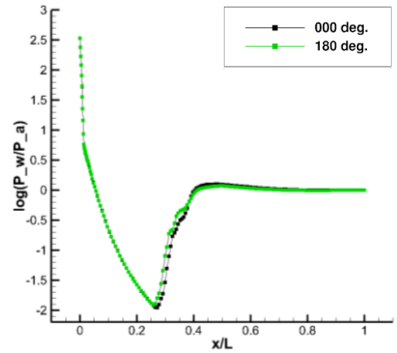
30	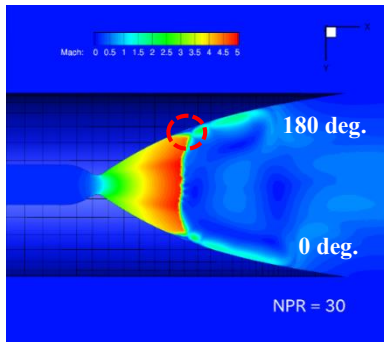	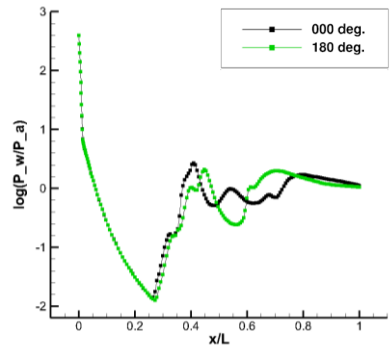

Figure 5.4: 3-D Mach contours and wall pressure profiles during start-up

5.1.3 Transition NPR range comparison

It was identified that the transition NPR between axisymmetric two - dimensional and the three - dimensional analysis results are different. However,

comparing the flow separation positions where transitions occur, it can be confirmed that the transition position in axisymmetric two-dimensional result is similar to those in three dimensions. As can be seen in Fig 5.5, in the three-dimensional case, the development of the internal flow is slower than in the two-dimensional case although the pressure ratio is increased in the same speed. Therefore, this means that three-dimensional flow development is delayed compared to the axisymmetric two-dimensional case for some reasons.

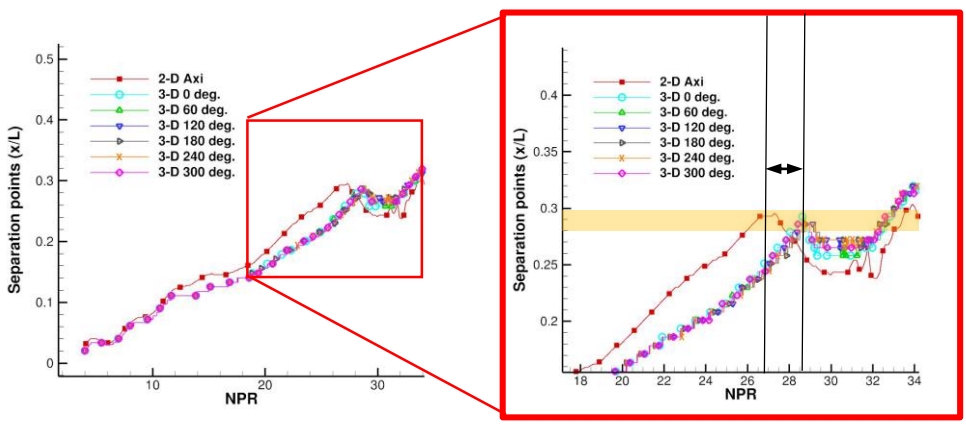

Figure 5.5: Separation position with NPR variation of 2-D and 3-D cases

To verify this, circumferential velocity component of the cross section at the point near the flow separation point are displayed. Figure 5.6 shows the circumferential velocity distribution on x/L≈ 0.30 at FSS and RSS state. As a result of analysis, it was verified that momentum was not transferred entirely to the axial velocity component, and some energy was used for the circumferential velocity component in three-dimensional cases. Therefore, in two-dimensional case, all energy was propagated along the axial direction to develop flow, but in contrast in

three-dimensional case, energy loss to the circumferential direction suppresses development of flow.

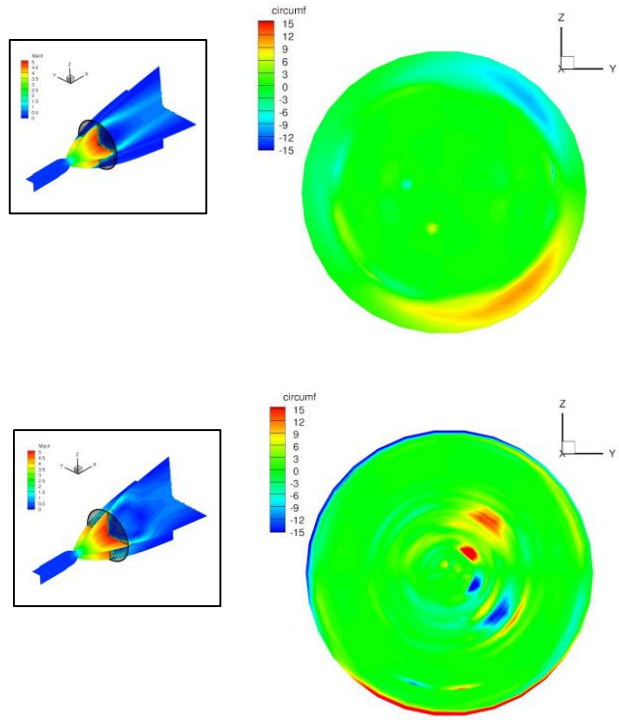

Figure 5.6: Circumferential velocity distribution on x/L≈ 0.30 at FSS (top) and RSS (bottom) state

5.2 Asymmetrical Wall Temperature Distribution in 3-D

In two-dimensional axisymmetric analysis, the wall surface temperature is similar to the external gas level in the FSS state because external gas enters the nozzle along the inner wall and flows out with the separated flow (see Fig. 5.7). But in the RSS, the wall surface temperature was relatively high from the separation point to the point where the large swirl behind the shock ends from the wall (see Fig. 5.8). The reason is that a high temperature flow formed in separation bubble leaks along the wall and this phenomenon lasts until the vortex behind the

swirl ends.

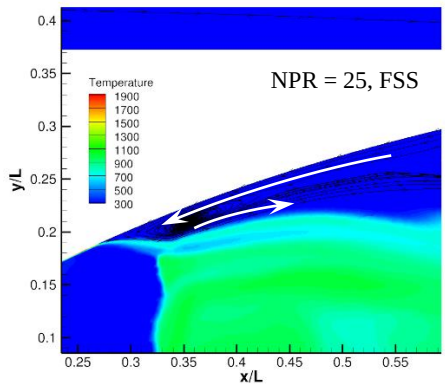

Figure 5.7: Temperature contour of FSS state

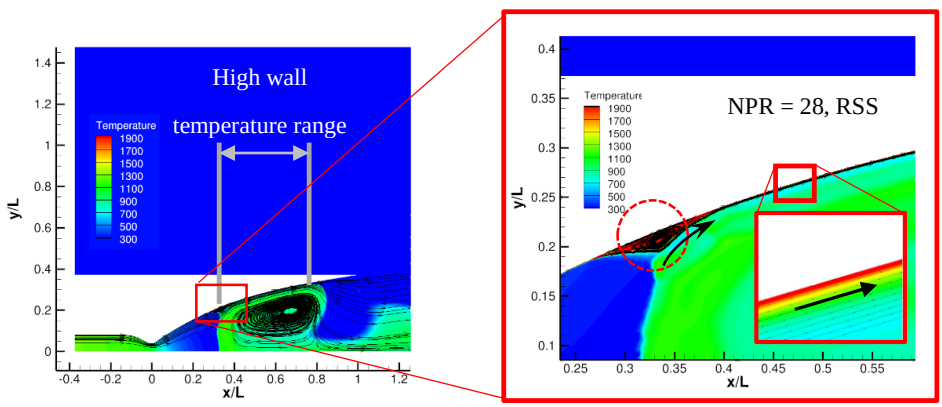

Figure 5.8: Temperature contour of RSS state

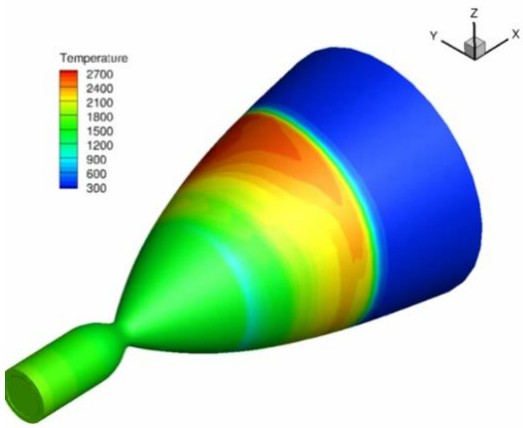

Figure 5.9: Surface temperature distribution on the nozzle wall

In three-dimensional flow analysis, the wall surface temperature was distributed asymmetrically. Observing the temperature distribution of the cross section of this result, the wall temperature at opposite phases are different and they are closely related to the flow leaking from the separation bubble as well as described in 2-D. In Fig 5.10, a separation bubble at the bottom (0 deg.) was formed relatively earlier than the opposite one (180 deg.), and it reaches higher temperature within the same time. And due to this, nozzle wall surface temperature was distributed asymmetrically.

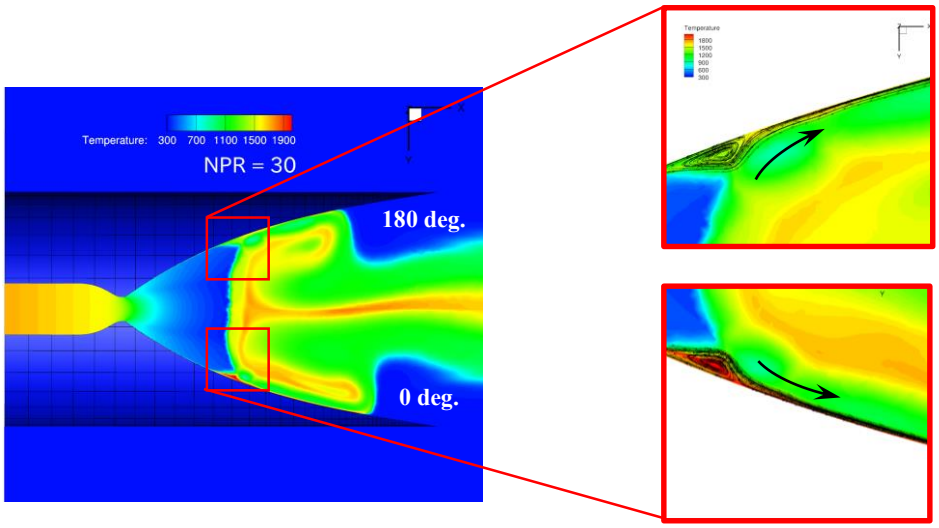

Figure 5.10: Asymmetrical nozzle temperature contour

Although it was impossible to clearly investigate the reason why the formation speed of separation bubble is different for each place, it can be inferred that the turbulence effect and the unstable interference occurring between the shock wave and the boundary layer may affect.

5.3 Side-load by Asymmetrical Pressure Distribution in 3-D

In the initial FSS state, generally symmetrical wall pressure was distributed so the side load and the lateral moment remained very weak. However, when the asymmetric wall pressure distribution begins with the transition to RSS occurs, about 3500 N of maximum side load and 2700 $N \cdot m$ of maximum moment on the neck of the nozzle appeared

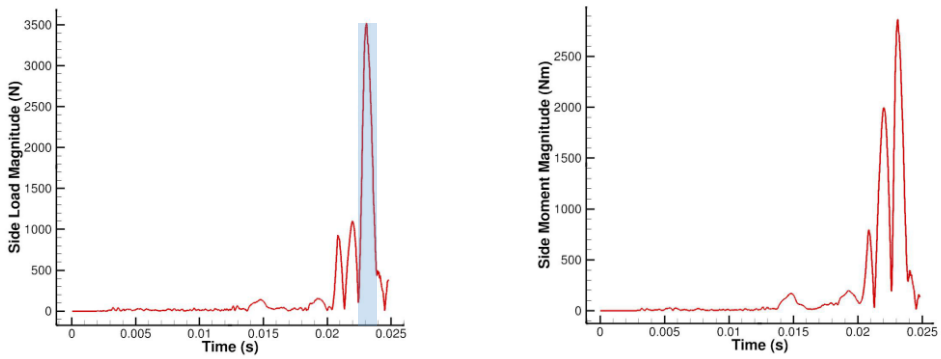

Figure 5.11: Side load magnitude ($|F|$) and moment magnitude ($|M|$) change

When the maximum side load was applied (highlighted region in Fig. 5.11), impulse value was about 4 N. However, considering that the very short loading time ($\approx 0.002s$), it was confirmed that the impact force is a considerable level of 175 t/s.

In order to analyze the asymmetry of such pressure distribution, the section near the shock wave at the moment when the side load was the maximum was observed (see Fig 5.12). As a result of observation, it was confirmed that the velocity component was deflected in one specific direction. The circumferential velocity component acting at this time was 482.3 m/s in the clockwise direction and 485.5 m/s in the counterclockwise direction. And 481.1 m/s of radial velocity component toward the axial center direction and 1077.3 m/s in the outward direction was applied.

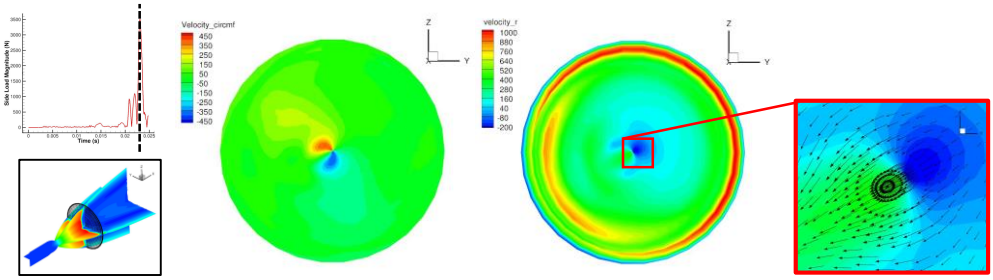

Figure 5.12: Circumferential (left) and radial (right) direction velocity distribution (x/L≈ 0.4)

Chapter 6

Conclusions

In this research, URANS two-dimensional axisymmetric and three-dimensional CFD analysis were conducted for start-up process considering pressure-time increment using structured-unstructured mixed grid system. The internal flow of the nozzle and the numerical three-dimensional effects were analyzed around the Nozzle Pressure Ratio (NPR) range when a transition from FSS to RSS occurs. The experimental data in this research is the result from our joint research institute, and based on the data provided, the following contents were confirmed.

Comparing the transition NPR Range between 2-D & 3-D cases, it was identified that the 3-D case showed slower flow development and separation pattern transition than the 2-D axisymmetric case because of the energy loss by the velocity component of circumferential direction. Also, it was observed that the wall temperature distribution is asymmetrically displayed by the different speed of separation bubble formation which presumed to be caused by the turbulence effect and the like. Finally, specific values of maximum side-load (3500 N) and moment (2700 Nm) acting by asymmetric wall pressure distribution were confirmed.

As a future work, it is necessary to investigate the exact cause of the

hysteresis phenomenon in which the transition NPR between FSS - RSS occurring in the nozzle at the time of starting and ending of the rocket engine is displayed differently.

Chapter 7

References

[1] Watanabe, Y., Sakazume, N., and Tsuboi, M., “LE-7A Engine Nozzle Problems During the Transient Operations,” AIAA Paper 2002-3841, July 2002.

[2] Winterfeldt, L., Laumert, B., Tano, R., Geneau, J. F., Blasi, R., and Hagemann, G., “Redesign of the Vulcain 2 Nozzle Extension,” AIAA Paper 2005-4536, Tucson, AZ, 2005.

[3] Nave, L. H., and Coffey, G.A., “Sea-level side-loads in high-area ratio rocket engines,” AIAA Paper No. 73-1284, 1973.

[4] Ostlund, J., “Flow Processes in Rocket Engine Nozzles with Focus On Flow Separation and Side-loads,” Ph.D. dissertation, KTH Royal Institute of Technology, 2002.

[5] Menter, F. R., “Two-Equation Eddy-Viscosity Turbulence Model for Engineering Applications,” AIAA Journal, Vol. 32, No. 8, 1994, pp. 1598, 1605.

[6] Kim, S.-s., Kim, C., Rho, O. H., and Kyu Hong, S., “Cures for the shock instability: development of a shock-stable Roe scheme,” Journal of Computational Physics, Vol. 185, No. 2, 2003, pp. 342, 374.

[7] Van Leer, B., “Towards the Ultimate Conservative Difference Scheme. V. A Second Order Sequel to Godunov’s Methods,” Journal of Computational Physics, Vol. 32, No. 1, 1979, pp. 101, 103.

[8] Yoon, S., and Jameson, A., “Lower-Upper Symmetric-Gauss-Seidel Method for the Euler and Navier-Stokes Equations,” AIAA Journal, Vol. 26, No. 9, 1988, pp. 1026, 1026.

[9] Hagemann, G., and Frey, M., "Shock pattern in the plume of rocket nozzles: needs for design consideration," Shock Waves, No. 17, 2008, pp. 387, 395.

[10] Schulein, E., Krogmann, P., and Stanewsky, E., "Documentation of Two-Dimensional Impinging Shock/Turbulent Boundary Layer Interaction Flow," DLR Report DLR IB 223-96 A 49, 1996.

[11] Seiner, J. M., Ponton, M. K., Jansen, B. J., and Lagen, N. T., "The Effect of Temperature on Jet Noise Emission," AIAA Paper 92-02-046,1992.

[12] Wang, T., Zhao, X, Zhang. S, and Chen, Y., "Development of an Aeroelastic Modeling Capability for Transient Nozzle Flow Analysis," Journal of Propulsion and Power, Vol. 30, No.6, 2014, pp 1692, 1700.

국문 초록

액체로켓 시동 과정에서 과 팽창 초기 상태로 진행되는 내부 유동은 유동 박리가 벽면에서 떨어져 있는 자유 충격파 박리 (Free Shock Separation, FSS) 상태로 유동이 발달하기 시작한다. 그러나 노즐 형상의 종류에 따라 유동 박리가 벽면에 재 부착되는 제한 충격파 박리 (Restricted Shock Separation, RSS) 상태로의 격동적이고 예측 불가능한 천이가 발생하게 된다.

본 연구에서는 정렬-비 정렬 혼합 격자 계 기반의 2 차원 축 대칭 및 3 차원 노즐 내부 유동에 대한 비정상 점성 해석을 CFD 시뮬레이션을 이용하여 수행 하였다. 특히 FSS 에서 RSS 로의 천이가 발생하는 노즐 압력 비(Nozzle Pressure Ratio, NPR) 구간을 중심으로 3 차원 효과를 분석하였다. 그 결과 노즐 압력 비가 증가함에 따라 축 대칭 2 차원 유동 해석 결과에 비해 3 차원의 경우 에서 천이가 더 늦게 발생하는 것으로 확인되었다. 또한 노즐 벽면 온도 비대칭 현상이 확인되어 그에 대한 원인을 분석하였으며, 노즐 벽면 비대칭 압력 분포에 의해 발생하는 측면 하중과 노즐 목에 작용하는 모멘트의 크기를 측정하였다.

주요어: 전산유체역학(CFD), 로켓 노즐, 과 팽창 유동, 자유 충격파 박리, 제한 충격파 박리, 3 차원 효과, 측면 하중

학 번: 2015-20768